Hybrid modeling network for a helium–argon–copper hollow cathode discharge used for laser applications

Annemie Bogaerts[a] and Renaat Gijbels
Department of Chemistry, University of Antwerp, Universiteitsplein 1, B-2610 Wilrijk-Antwerp, Belgium

(Received 5 June 2002; accepted 5 September 2002)

A hybrid modeling network, consisting of several Monte Carlo and fluid models, is developed for a hollow cathode glow discharge in a mixture of helium and argon, with copper as the cathode material. The species considered in the models are the helium and argon gas atoms, electrons, He^+, He_2^+, Ar^+, and Ar_2^+ ions, He and Ar metastable atoms, fast He and Ar atoms, and sputtered Cu atoms and Cu^+ ions. The modeling network is applied to typical laser conditions. The results of the model, presented in this article, include the electric potential distribution, the density profiles of the various plasma species, and the relative contributions of the various production and loss mechanisms for the plasma species. The model gives us more insight into the plasma behavior, and is therefore useful for optimization of the discharge efficiency for laser applications. © *2002 American Institute of Physics.* [DOI: 10.1063/1.1517751]

I. INTRODUCTION

Hollow cathode discharges (HCDs) are used for various applications, such as lasers,[1,2] atomic spectrometry,[3,4] and plasma processing (ion etching, thin-film deposition, surface treatment).[5] To improve the results in these applications, insight into the discharge behavior is desirable. In this article, we present a comprehensive modeling network for a HCD used for laser applications. Cu is chosen as the cathode material, and the discharge operates in a mixture of He with Ar. The combination of He/Cu gives rise to a 780.78 nm CuII laser line, produced by asymmetric charge transfer between He^+ ions and Cu atoms. Ar is added to the He gas to promote sputtering of the Cu cathode.[6–12]

There exist a number of models in the literature for HCDs used as metal vapor ion lasers.[10,13–19] However, most of these models consider only buffer gas ions, sputtered metal vapor atoms, and corresponding ions, such as for a Cu–Ne laser.[13–17] A few models presented in the literature take into account more species. In Ref. 18, a model is developed for a He–Hg HCD, which calculates the electron energy distribution function (EEDF), the densities of He^+ and Hg^+ ions, and of 12 states of He and Hg. Moreover, it contains rate equations for the upper and lower laser levels, and calculates the laser power and optical gain. Another comprehensive model is described by Bánó *et al.* for a segmented HCD in He–Ar with Au sputtering.[19] It consists of Monte Carlo models for the electrons, and for the He^+, Ar^+, and Au^+ ions and fast He^0 and Ar^0 atoms in the cathode dark space, as well as a fluid model with rate equations for He^+, Ar^+, Au^+, He*, and Au, and a heat conduction model to calculated the gas temperature. In Ref. 10, a model is reported for a He–Ar–Cu HCD, based on the Boltzmann equation, to calculate the EEDF, and balance equations for the He^+, Ar^+, and Cu^+ ions, the sputtered Cu atoms, and the He and Ar metastable atoms. However, at the typical laser conditions of interest here, i.e., a pressure of several Torr and an electrical current of several A, also He_2^+ and Ar_2^+ ions come into play.[20–22] Moreover, fast He and especially Ar atoms are expected to play a non-negligible role in the sputtering process. Therefore, our model for the He–Ar–Cu HCD takes into account the following plasma species: helium and argon gas atoms, electrons, He^+, He_2^+, Ar^+, and Ar_2^+ ions; He and Ar metastable atoms (He_m* and Ar_m*); fast He and Ar atoms; and sputtered Cu atoms and Cu^+ ions. These species are described with a combination of several Monte Carlo and fluid models. In Sec. II, these models will be described in some detail, and the coupling of the models will be outlined. The results of the model will be presented in Sec. III, and it will be demonstrated how these results give us a better insight into the behavior of the discharge and the laser. Finally, the conclusion will be given in Sec. IV.

II. DESCRIPTION OF THE MODELS

An overview of the various species assumed to be present in the plasma, and of the models used to describe these species, is given in Table I. No specific model is applied to the He and Ar gas atoms. Indeed, these species are assumed to be uniformly distributed in the plasma and with thermal velocities. The other species are described with Monte Carlo and fluid models. Briefly, the fast plasma species (such as fast electrons, which are not in equilibrium with the electric field) are treated with Monte Carlo simulations, whereas a fluid approach is applied for the slow plasma species (such as the slow electrons, which can be considered in equilibrium with the electric field, as well as the neutral species). As appears from Table I, the He^+, Ar^+, and Cu^+ ions are described both with Monte Carlo and fluid models (see below). The models will be applied to a HCD with 5 cm length and 4 mm inner diameter. The Monte Carlo models are developed in three dimensions, whereas the fluid models

[a]Author to whom correspondence should be addressed; electronic mail: annemie.bogaerts@ua.ac.be

TABLE I. Species assumed to be present in the plasma, and models used to describe their behavior.

Plasma species	Model
He gas atoms	No model (assumed to be thermal and uniformly distributed)
Ar gas atoms	
Fast electrons	Monte Carlo model
Slow electrons	Fluid model
He^+ ions	Fluid model
He_2^+ ions	Fluid model
Ar^+ ions	Fluid model
Ar_2^+ ions	Fluid model
Metastable He atoms (He_m*)	Fluid model
Metastable Ar atoms (Ar_m*)	Fluid model
He^+ ions	Monte Carlo model
Ar^+ ions	Monte Carlo model
Fast He atoms	Monte Carlo model
Fast Ar atoms	Monte Carlo model
Sputtering of Cu cathode	Empirical formula
Thermalization of sputtered Cu atoms	Monte Carlo model
Thermal Cu atoms	Fluid model
Cu^+ ions	Fluid model
Cu^+ ions	Monte Carlo model

are applied in two dimensions (axial and radial directions), due to the cylindrical symmetry of the discharge cell. The different models will be outlined below.

A. Monte Carlo model for fast electrons

The electrons are split up into two groups, depending on their energy. Electrons with total energy (i.e., sum of potential and kinetic energies) above the threshold for inelastic collisions with the He and Ar atoms, are called ''fast'' and are simulated with a Monte Carlo (MC) model.

The electrons start at the cathode, as a result of secondary electron emission. We use constant secondary electron emission coefficients (i.e., independent of the bombarding energy) equal to 0.06 for the Ar^+ ions and 0.3 for the He^+ ions. The fast He and Ar atoms are assumed not to contribute to the secondary electron emission. These assumptions are characteristic for so-called ''potential electron ejection,'' which is a reasonable assumption here, because the cathode surface will be kept ''clean'' by sputtering. The contributions of He_2^+ and Ar_2^+ ions to the secondary electron emission are at first neglected, which is justified by their lower fluxes.

The electrons are accelerated away from the cathode by the electric field. Their trajectory during successive time steps is calculated by Newton's laws, and the collisions during these time steps (i.e., occurrence of a collision, kind of collision, and new energy and direction after collision) are treated with random numbers, in analogy to our previously developed electron MC models.[23,24] The collision processes taken into account here are elastic collisions with He and Ar gas atoms, ionization and excitation of He and Ar ground state atoms, ionization and excitation of the Ar metastable atoms, ionization of the He metastable atoms, and ionization of sputtered Cu atoms. It is worth mentioning that collisions with He and Ar ground state gas atoms occur much more often than the other collision processes, due to the high He and Ar gas atom densities. Hence, these collisions are by far the most important in determining the electron energy. The other processes taken into account in the electron MC model do not occur very often and they do not affect the electron energy to a large extent; they are only included because they determine the He and Ar metastable densities and the Cu atom and Cu^+ ion densities (see below). Excitation of the He metastable atoms is not incorporated in the MC model, because this process is not included in the He metastable model either (see below). Indeed, electron excitation to the higher He excited levels is almost immediately followed by radiative decay back to the metastable levels, so that it has no effect on the He metastable population density.[20] Also, electron impact excitation of the sputtered Cu atoms is not taken into account in the electron MC model, because this process does not affect the electron energy, and here we are not interested in the Cu atom excited levels.

The cross sections of the electron processes, as used in our model, are adopted from Refs. 25–32, and are plotted as a function of electron energy in Figs. 1(a) and 1(b). Besides the total excitation cross sections from He and Ar ground-state atoms, also the cross sections for excitation from the ground states to the He and Ar metastable levels are shown. These processes are also explicitly treated in the model (as part of the total excitation mechanisms), because they are important for determining the metastable level populations (see below).

When the total (kinetic+potential) energy of the electrons drops below the threshold for inelastic collisions [i.e., 1.8 eV; for excitation from the Ar metastable level; see Fig. 1(b)], the electrons are transferred to the slow electron group, which is treated in the fluid model. Indeed, these electrons cannot give rise to inelastic collisions anymore; their only role in the plasma is to provide negative space charge and to carry electrical current, and this can as well be described in the fluid code. It should be mentioned that this transfer to the slow electron group occurs only in the negative glow (NG), where the electric field is weak and hence the potential energy of the electrons is low. Hence, slow electrons exist only in the NG; their density is negligible in the cathode dark

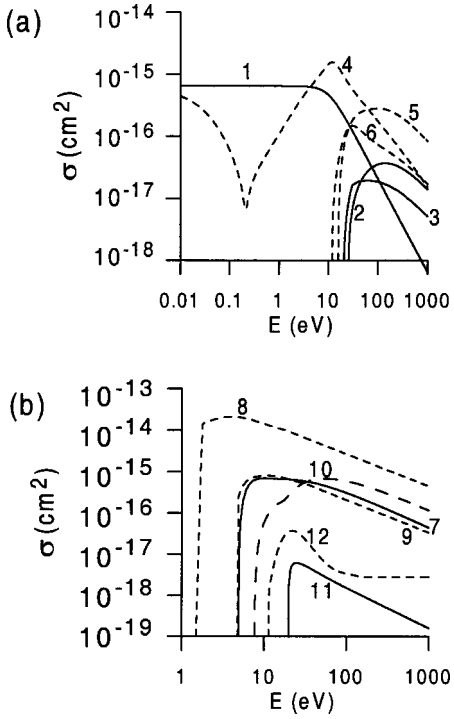

FIG. 1. Cross sections of the electron reactions as a function of the electron energy. (a) shows the most important reactions with He ground-state atoms (solid lines) and Ar ground-state atoms (dashed lines): (1) elastic collisions with He atoms (see Ref. 26), (2) electron impact ionization of He ground state atoms (see Ref. 26), (3) total electron impact excitation of He ground-state atoms (see Ref. 27), (4) elastic collisions with Ar atoms (see Ref. 28), (5) electron impact ionization of Ar ground state atoms (see Ref. 28), (6) total electron impact excitation of Ar ground-state atoms (see Ref. 28). (b) illustrates the electron reactions which do not occur so often, i.e., with He_m* or Ar_m* metastable atoms or sputtered Cu atoms, as well as electron impact excitation to the He_m* or Ar_m* metastable level. The cross sections with respect to He, Ar, and Cu are plotted with solid, short-dashed, and wide-dashed lines, respectively: (7) electron impact ionization from the He_m* metastable level (see Ref. 25), (8) total electron impact excitation from the Ar_m* metastable level (see Ref. 29), (9) electron impact ionization from the Ar_m* metastable level (see Ref. 30), (10) electron impact ionization of the sputtered Cu atoms (see Ref. 31), (11) electron impact excitation from the He ground state to the He_m* metastable level (see Ref. 32), (12) electron impact excitation from the Ar ground state to the Ar_m* metastable level (see Ref. 32).

space (CDS), where a strong electric field is present.

B. Fluid model for slow electrons, He^+, He_2^+, Ar^+, and Ar_2^+ ions

Because the slow electrons and the He^+, He_2^+, Ar^+, and Ar_2^+ ions can be considered more or less in equilibrium with the electric field (i.e., the energy gain from the electric field is compensated by energy losses due to collisions), they are treated with a fluid model. It consists of the following equations:

• Five continuity equations, for the electrons and the various ions, with different production and loss terms:

$$\frac{\partial n_x}{\partial t} + \overline{\nabla} \cdot \overline{j_x} = R_{\text{prod},x} - R_{\text{loss},x}.$$

• Five transport equations for these five different species, based on migration in the electric field (first term) and on diffusion (second term):

$$\overline{j_x} = \pm \mu_x n_x \overline{E} - D_x \overline{\nabla} n_x.$$

• Moreover, these ten equations are coupled to Poisson's equation, for a self-consistent calculation of the electric field distribution (based on the densities of the charged species):

$$\overline{\nabla} \cdot \overline{E} = \frac{e}{\varepsilon_0}(n_{He^+} + n_{He_2^+} + n_{Ar^+} + n_{Ar_2^+} - n_e).$$

In these equations, n and j denote the particle density and flux, respectively; x stands for each of the five different species; R_{prod} and R_{loss} are the total production and loss rates; E is the electric field distribution; and μ and D symbolize the mobility and diffusion coefficients of the various species. In the transport equation, a positive sign in the migration term is used for the ions, whereas a negative sign applies to the electrons.

The mobility and diffusion coefficients of the electrons are assumed to be[33] $3\times10^5\ \text{cm}^2\,\text{s}^{-1}$ and $1.2\times10^6\ \text{cm}^2\,\text{s}^{-1}\,\text{V}^{-1}$ at 1 Torr, respectively. The mobilities of the ionic species in the He/Ar gas mixture are calculated from the values in the pure gases, according to Blanc's law:[34]

$$\mu_{AB} = \frac{\mu_A \mu_B}{f_A \mu_B + f_B \mu_A},$$

where μ_A, μ_B, and μ_{AB} are the ion mobility in gas A, gas B, and gas mixture $A+B$, respectively; and f_A and f_B are the fractional concentrations of gases A and B in the gas mixture. The same formula is also used for the ion diffusion coefficients in the gas mixture.

The mobilities of He^+ and Ar^+ ions in both pure gases He and Ar, as a function of reduced electric field strength, are adopted from Ref. 35, whereas the diffusion coefficients of He^+ and Ar^+ ions in the pure gases He and Ar, are calculated from rigid sphere theory.[36] This is an approximation, in view of the polarization interaction, but it is justified, because the model is also subject to many other uncertainties in the input data. This makes exact quantitative predictions not yet possible, but the modeling results can certainly give more insight into the discharge behavior. Finally, the mobilities and diffusion coefficients of He_2^+ and Ar_2^+ ions are taken from Refs. 20 and 37, respectively.

The production and loss processes taken into account for the different species are summarized in Table II. The rates of these processes are either calculated in the fluid model itself (based on the rate coefficients and the densities of the reacting species) or they are obtained from the other models. Hence, Table II includes also the rate coefficients (for the rates calculated in the fluid model itself) or it gives the models where the rates are obtained from.

Although the core of the fluid model (i.e., type of equations and solution algorithm based on the Scharfetter–Gummel exponential scheme[38]) is the same as for the electron–Ar^+ ion fluid model developed previously,[24] the present fluid model contains many more production and loss processes. Indeed, not only He^+ ions are added to the model,

TABLE II. Production and loss processes for the slow electrons, He^+, He_2^+, Ar^+, and Ar_2^+ ions, described in the fluid model. Also given are the models where the rates are taken from, or the rate coefficients (if the rates are calculated in the fluid model itself), and the references of these data.

Production of electrons		
Transfer to the slow electron group	$e^-_{fast} \rightarrow e^-_{slow}$	From electron MC model
Collisions between two He_m* atoms, leading either to ionization of one of the atoms, or to associative ionization	$He_m^* + He_m^* \rightarrow He^+ + He^0 + e^-$ or $He_2^+ + e^-$	From He_m* model
Collisions between two Ar_m* atoms, leading either to ionization of one of the atoms, or to associative ionization	$Ar_m^* + Ar_m^* \rightarrow Ar^+ + Ar^0 + e^-$ or $Ar_2^+ + e^-$	from Ar_m* model
Associative ionization from He excited levels	$He^{**} + He \rightarrow He_2^+ + e^-$	$k = 8\times10^{-11}$ cm^3 s^{-1} (Ref. 21)
Associative ionization from Ar excited levels	$Ar^{**} + Ar \rightarrow Ar_2^+ + e^-$	From Ar_m* model
Penning ionization of Ar atoms by He_m* atoms	$He_m^* + Ar^0 \rightarrow He^0 + Ar^+ + e^-$	From He_m* model
Penning ionization of Cu atoms by He_m* atoms	$He_m^* + Cu^0 \rightarrow He^0 + Cu^+ + e^-$	From He_m* model
Penning ionization of Cu atoms by Ar_m* atoms	$Ar_m^* + Cu^0 \rightarrow Ar^0 + Cu^+ + e^-$	From Ar_m* model
Loss of electrons		
Three-body recombination with He^+ ions (with electron as the third body)	$He^+ + e^- + e^- \rightarrow He + e^-$	$k = 6\times10^{-20}$ cm^6 s^{-1} (Ref. 20)
Three-body recombination with He_2^+ ions (with electron as the third body)	$He_2^+ + e^- + e^- \rightarrow He_2^* + e^-$	$k = 4\times10^{-20}$ cm^6 s^{-1} (Ref. 20)
Three-body recombination with He_2^+ ions [with He (or Ar) gas atoms as the third body]	$He_2^+ + e^- + He \rightarrow He_2^* + He$	$k = 5\times10^{-27}$ cm^6 s^{-1} (Ref. 20)
Three-body recombination with Ar^+ ions (with the electron as the third body)	$Ar^+ + e^- + e^- \rightarrow Ar + e^-$	$k = 5.4\times10^{-27} T_e^{-9/2}$ cm^6 s^{-1} (Ref. 45)
Three-body recombination with Ar^+ ions [with Ar (or He) gas atoms as the third body]	$Ar^+ + e^- + Ar \rightarrow Ar + Ar$	$k = 10^{-11} * p$ (Torr) cm^3 s^{-1} (Ref. 46)
Radiative recombination with Ar^+ ions	$Ar^+ + e^- \rightarrow Ar + h\nu$	$k = 10^{-11}$ cm^3 s^{-1} (Ref. 47)
Dissociative recombination with Ar_2^+ ions	$Ar_2^+ + e^- \rightarrow Ar + Ar$	$k = 8.5\times10^{-7}(T_e/300)^{-0.67}(T_g/300)^{-0.58}$ cm^3 s^{-1} (Ref. 48)
Production of He^+ ions		
Electron impact ionization from He^0 or He_m* atoms	He^0(or He_m^*) $+ e^- \rightarrow He^+ + 2\,e^-$	From electron MC model
Collisions between two He_m* atoms, leading to ionization of one of the atoms	$He_m^* + He_m^* \rightarrow He^+ + He^0 + e^-$	From He_m* model
Loss of He^+ ions		
Three-body recombination with two electrons	$He^+ + e^- + e^- \rightarrow He + e^-$	$k = 6\times10^{-20}$ cm^6 s^{-1} (Ref. 20)
Asymmetric charge transfer with Cu atoms	$He^+ + Cu^0 \rightarrow He^0 + Cu^+$	$k = 3.47\times10^{-11} T_g^{1/2}$ cm^3 s^{-1} (Ref. 10)
Conversion into He_2^+ ions	$He^+ + 2\,He \rightarrow He_2^+ + He$	$k = 67$ Torr^{-2} s^{-1} (Ref. 20)
Production of He_2^+ ions		
Conversion from He^+ ions	$He^+ + 2\,He \rightarrow He_2^+ + He$	$k = 67$ Torr^{-2} s^{-1} (Ref. 20)
Collisions between two He_m* atoms, leading to associative ionization	$He_m^* + He_m^* \rightarrow He_2^+ + e^-$	From He_m* model
Associative ionization from higher excited levels	$He^{**} + He \rightarrow He_2^+ + e^-$	$k = 8\times10^{-11}$ cm^3 s^{-1} (Ref. 21)
Loss of He_2^+ ions		
Three-body recombination with two electrons	$He_2^+ + e^- + e^- \rightarrow He_2^* + e^-$	$k = 4\times10^{-20}$ cm^6 s^{-1} (Ref. 20)
Three-body recombination with one electron and a gas atom as third body	$He_2^+ + e^- + He \rightarrow He_2^* + He$	$k = 5\times10^{-27}$ cm^6 s^{-1} (Ref. 20)
Production of Ar^+ ions		
Electron impact ionization from Ar^0 or Ar_m* atoms	Ar^0(or Ar_m^*) $+ e^- \rightarrow Ar^+ + 2\,e^-$	From electron MC model
Collisions between two Ar_m* atoms, leading to ionization of one of the atoms	$Ar_m^* + Ar_m^* \rightarrow Ar^+ + Ar^0 + e^-$	From He_m* model
Penning ionization of Ar atoms by He_m* atoms	$He_m^* + Ar^0 \rightarrow He^0 + Ar^+ + e^-$	From He_m* model
Loss of Ar^+ ions		
Three-body recombination with two electrons	$Ar^+ + e^- + e^- \rightarrow Ar + e^-$	$k = 5.4\times10^{-27} T_e^{-9/2}$ cm^6 s^{-1} (Ref. 45)
Three-body recombination with one electron and a gas atom as the third body	$Ar^+ + e^- + Ar \rightarrow Ar + Ar$	$k = 10^{-11} * p$ (Torr) cm^3 s^{-1} (Ref. 46)
Radiative recombination with an electron	$Ar^+ + e^- \rightarrow Ar + h\nu$	$k = 10^{-11}$ cm^3 s^{-1} (Ref. 47)
Asymmetric charge transfer with Cu atoms	$Ar^+ + Cu^0 \rightarrow Ar^0 + Cu^+$	$k = 10^{-11} T_g^{1/2}$ cm^3 s^{-1} (Ref. 10)
Conversion into Ar_2^+ ions	$Ar^+ + 2\,Ar \rightarrow Ar^+_2 + Ar$	$k = 2.7\times10^{-31}$ cm^6 s^{-1} (Ref. 49)
Production of Ar_2^+ ions		
Conversion from Ar^+ ions	$Ar^+ + 2\,Ar \rightarrow Ar^+_2 + Ar$	$k = 2.7\times10^{-31}$ cm^6 s^{-1} (Ref. 49)
Collisions between two Ar_m* atoms, leading to associative ionization	$Ar_m^* + Ar_m^* \rightarrow Ar_2^+ + e^-$	From Ar_m* model
Associative ionization from higher excited levels	$Ar^{**} + Ar \rightarrow Ar_2^+ + e^-$	From Ar_m* model
Loss of Ar_2^+ ions		
Dissociative recombination with electrons	$Ar_2^+ + e^- \rightarrow Ar + Ar$	$k = 8.5\times10^{-7}(T_e/300)^{-0.67}(T_g/300)^{-0.58}$ cm^3 s^{-1} (Ref. 48)

but also Ar_2^+ and He_2^+ ions, which become important at the high pressures typical for laser applications (see below). Consequently, a number of processes yielding production of these species has to be described in the model, such as conversion from atomic (He^+ and Ar^+) ions to molecular (He_2^+ and Ar_2^+) ions by collisions with two gas atoms, and associative ionization. The latter process can occur by collisions of two (identical) metastable atoms (He_m* or Ar_m*, respectively) or by collisions of higher excited (He* or Ar*) levels with He or Ar ground-state atoms (so-called ''Hornbeck–Molnar associative ionization''). The rate of associative ionization by two metastable atoms is obtained from the metastable models (see below). To obtain the rate of Hornbeck–Molnar associative ionization, the population density of the excited levels with energy above 22.4 eV for He and 14.7 eV for Ar (i.e., which corresponds to the ionization threshold for He_2^+ and Ar_2^+, respectively[39,40]), should be known. This is typically calculated in so-called collisional–radiative models. However, in order not to further complicate the present modeling network, such collisional–radiative models are not developed for the present gas mixture. Hence, we have to make some guesses for the rates of Hornbeck–Molnar associative ionization.

For argon, a collisional–radiative model describing the behavior of 64 Ar excited levels, was previously developed,[41] and the process of Hornbeck–Molnar associative ionization for all levels above 14.7 eV, was explicitly taken into account as the production mechanism for Ar_2^+ ions.[37] It was found that the rates of Hornbeck–Molnar and metastable–metastable associative ionization were comparable to each other.[37] Hence, in the present model we simply assume the rate of Hornbeck–Molnar associative ionization being equal to the rate of metastable–metastable associative ionization, which is calculated in the Ar metastable model (see below).

For helium, no collisional–radiative model for He excited levels has been developed previously, but the rate of Hornbeck–Molnar associative ionization is estimated in the following way.[21] The population density of He excited levels with $n \geqslant 3$ (i.e., energy above 22.4 eV) is simply calculated by

$$n_{\mathrm{He}*}(z,r) = \frac{S_{\mathrm{He}*}(z,r)}{\frac{1}{\tau} + k_{\mathrm{ass.ion.}} n_{\mathrm{He}}},$$

where $S_{\mathrm{He}*}(z,r)$ is the rate of electron impact excitation to all He excited levels with $n \geqslant 3$. It is calculated in the electron MC model, with a cross section equal to the sum of excitation to all levels with n equal to 3, 4, or 5, which is adopted from Ref. 42. Excitation to higher excited levels is neglected, because of the lower cross sections.[42,43] Further, τ is the overall lifetime of these excited levels, which is obtained from the natural lifetime (τ_0) and the so-called collision lifetime (τ_p), which is inversely proportional to the pressure:

$$\frac{1}{\tau} = \frac{1}{\tau_0} + \frac{1}{\tau_p} = \frac{1}{\tau_0} + \frac{p}{A}.$$

τ_0 is equal to 217 ns,[44] p is the pressure (in Torr), and the constant A is assumed equal to 400, which gives values for τ in agreement with tabulated values in a wide pressure range.[44] Finally, $k_{\mathrm{ass.ion.}}$ is the rate constant for Hornbeck–Molnar associative ionization of helium, which is taken as $8 \times 10^{-11}\ \mathrm{cm^3\ s^{-1}}$.[21,44] Based on the He excited level population, $n_{\mathrm{He}*}(z,r)$, computed in this way, the rate of Hornbeck–Molnar associative ionization is then calculated as

$$S_{\mathrm{ass.ion.}}(z,r) = k_{\mathrm{ass.ion.}} n_{\mathrm{He}*}(z,r) n_{\mathrm{He}}.$$

Another difference with the basic fluid model[24] is that recombination is included as a loss mechanism for the electrons and various ions.[45–49] Indeed, the basic fluid code was developed for glow discharges operating at typical currents of several mA, and recombination between electrons and (atomic) ions was found to be negligible. The HCD used for laser applications, on the other hand, operates at much higher current (order of several A). Consequently, the ions and electrons have higher densities, and ion–electron recombination cannot be neglected anymore. For Ar^+ ions, the three classical recombination mechanisms, i.e., three-body recombination with either an electron or a gas atom as the third body, and radiative recombination, are taken into account. For He^+ ions, it was found that only three-body recombination with an electron as the third body, is significant.[20,21] For Ar_2^+ ions, dissociative recombination is by far the dominant recombination mechanism,[37] whereas for He_2^+ ions, three-body recombination with either an electron and a gas atom as the third body, are important,[20,21] and dissociative recombination is negligible.[21]

Moreover, some additional production and loss mechanisms are included in this fluid model, which are related to the other plasma species described in the modeling network, i.e., Penning ionization by Ar and He metastable atoms and asymmetric charge transfer with sputtered Cu atoms.

Finally, it should be mentioned that there is one additional loss mechanism described in the model for all five species, i.e., diffusion toward and subsequent recombination at the cell walls.

As mentioned above, these coupled differential equations (continuity and transport equations, and Poisson equation) are solved simultaneously with the Scharfetter–Gummel exponential scheme.[24,38] It is worth mentioning that because of the nonlinearity and strong coupling of these equations, solving this fluid model is a difficult numerical task, and small time steps had to be used (order of 10^{-12} s). Therefore, this fluid model requires most of the calculation time of the entire modeling network (see below).

C. Fluid model for metastable He atoms (He_m*)

Because metastable He atoms might play an important role in the discharge, e.g., for production of Ar^+ and Cu^+ ions (by Penning ionization), they should be taken into account in a comprehensive modeling network.

Helium has two metastable levels, i.e., a triplet ($1s\,2s\,^3S_1$) level and a singlet ($1s\,2s\,^1S_0$) level, lying at 19.8 and 20.6 eV above the ground state, respectively. The triplet level appears to have a much higher population density.[50–52] Indeed, the singlet metastable level is rapidly

TABLE III. Production and loss processes for the He_m^* atoms. Also given are the models where the rates are taken from, or the rate coefficients (if the rates are calculated in the fluid model itself), and the references of these data.

Production of He_m^* atoms		
Electron impact excitation from He atoms	$He^0+e^-\rightarrow He_m^*+e^-$	From electron MC model
He^+/e^- three-body recombination	$He^++e^-+e^-\rightarrow He^*+e^-\rightarrow He_m^*+e^-$	$k=6\times10^{-20}$ cm^6 s^{-1} (Ref. 20)
He_2^+/e^- three-body recombination	$He_2^++e^-+e^-\rightarrow He_2^*+e^-\rightarrow He_m^*+He+e^-$ (prob: 0.7)	$k=0.7*4\times10^{-20}$ cm^6 s^{-1} (Ref. 20)
	$He_2^++e^-+He\rightarrow He_2^*+He\rightarrow He_m^*+He+He$ (prob: 0.7)	$k=0.7*5\times10^{-27}$ cm^6 s^{-1} (Ref. 20)
Loss of He_m^* atoms		
Electron impact ionization	$He_m^*+e^-\rightarrow He^++2\,e^-$	From electron MC model
Electron impact deexcitation	$He_m^*+e^-\rightarrow He+e^-$	$k=4.2\times10^{-9}$ cm^3 s^{-1} (Ref. 20)
Penning ionization of Ar atoms	$He_m^*+Ar^0\rightarrow He^0+Ar^++e^-$	$k=5.3\times10^{-12}T_g^{1/2}$ cm^3 s^{-1} (Ref. 10)
Penning ionization of sputtered Cu atoms	$He_m^*+Cu^0\rightarrow He^0+Cu^++e^-$	$k=3\times10^{-11}T_g^{1/2}$ cm^3 s^{-1} (ref. 10)
Two-body collisions with gas atoms, leading to deexcitation	$He_m^*+He\rightarrow He+He$	$k=6\times10^{-15}$ cm^3 s^{-1} (Ref. 53)
Three-body collisions with gas atoms, leading to He_2^*	$He_m^*+2\,He\rightarrow He_2^*+He$	$k=2.5\times10^{-34}$ cm^6 s^{-1} (Ref. 53)
Collisions between two He_m^* atoms, followed by ionization of one of the atoms	$He_m^*+He_m^*\rightarrow He^++He^0+e^-$ (prob: 0.3)	$k=0.3*2\times10^{-9}$ cm^3 s^{-1} (Refs. 20 and 51)
Collisions between two He_m^* atoms, followed by associative ionization	$He_m^*+He_m^*\rightarrow He_2^++e^-$ (prob: 0.7)	$k=0.7*2\times10^{-9}$ cm^3 s^{-1} (Refs. 20 and 51)

converted into the triplet level by collisions with electrons.[20] Since we are only interested in the role of He metastable atoms in general (e.g., for Penning ionization), and since it has been demonstrated[51] that the processes determining the triplet and singlet level populations are mostly similar, we have combined the two metastable levels into one effective level, lying at 19.8 eV above the ground state.

The He metastable atom density is calculated with a fluid model, which consists again of a continuity equation with different production and loss terms, and a transport equation based on diffusion:

$$\frac{\partial n_{\mathrm{He}_m^*}}{\partial t}+\overline{\nabla}\cdot\overline{j_{\mathrm{He}_m^*}}=\overline{R}_{\mathrm{prod,He}_m^*}-R_{\mathrm{loss,He}_m^*}$$

$$\overline{j_{\mathrm{He}_m^*}}=-D_{\mathrm{He}_m^*}\overline{\nabla}n_{\mathrm{He}_m^*}.$$

The symbols have the same meaning as above. The He_m^* diffusion coefficient is assumed to be 420 cm^2 s^{-1} at 1 Torr and 300 K, which is the value reported for the triplet level.[20] The production and loss processes taken into account in this model are presented in Table III,[20,51,53] together with the reaction rate coefficients or with the models where the rates are calculated from.

Beside electron impact excitation from the He ground state, also recombination of electrons with He^+ or He_2^+ ions leads to formation of the He_m^* metastable levels. It is stated[20] that 100% of the He^+–electron recombination and 70% of the He_2^+–electron recombination leads to He_m^*.

Concerning the loss mechanisms, electron impact excitation from the He metastable level to higher levels is not taken into account, as is mentioned above, because the higher levels would decay back radiatively to the triplet level, so that the net effect is zero.[51] Electron impact deexcitation, on the other hand, is taken into account. Because this process is induced by slow electrons (i.e., there is no high energy required), it is treated in the fluid model itself, using the rate coefficient and the density of the slow electrons (obtained from the electron–ion fluid model).

Collisions between two He_m^* atoms can lead either to ionization of one of the atoms, or to associative ionization. The total rate coefficient (for both reaction products) is assumed to be[51] 2×10^{-9} cm^3 s^{-1}, which is an average value for singlet and triplet levels. The probability for formation of He^+ and He_2^+ ions is taken as 0.3 and 0.7, respectively.[20,21]

D. Fluid model for metastable Ar atoms (Ar_m^*)

In analogy to the above model, a similar fluid model is developed for metastable Ar atoms. Again, there exist two Ar metastable levels lying close to each other, i.e., the $(3p^5\,4s)\,^3P_2$ level and the $(3p^5\,4s)\,^3P_0$ level, at 11.55 and 11.72 eV above the ground state, respectively. The $^3P_0$ level is stated to be populated by a fraction of 10%–20% of the $^3P_2$ level.[54,55] Since we are again only interested in the total metastable density, we have combined the two metastable levels in one collective level, lying at 11.55 eV. This model was developed previously,[56] but it contains some extra production and loss processes, relevant to the He–Ar HCD.

The behavior of Ar_m^* atoms is again described with a continuity equation and a transport equation based on diffusion:

$$\frac{\partial n_{\mathrm{Ar}_m^*}}{\partial t}+\overline{\nabla}\cdot\overline{j_{\mathrm{Ar}_m^*}}=\overline{R}_{\mathrm{prod,Ar}_m^*}-R_{\mathrm{loss,Ar}_m^*}$$

$$\overline{j_{\mathrm{Ar}_m^*}}=-D_{\mathrm{Ar}_m^*}\overline{\nabla}n_{\mathrm{Ar}_m^*}.$$

The Ar_m^* diffusion coefficient is taken to be 54 cm^2 s^{-1} at 1 Torr and 300 K.[57] The production and loss processes considered in this model, are given in Table IV,[58,59] together with the rate coefficients or with the models from which the rates are calculated.

Both electron impact ionization and excitation from the Ar_m^* metastable level are taken into account, as well as transfer to the nearby 4*s* resonant levels [i.e., the $(3p^5\,4s)\,^3P_1$ level and the $(3p^5\,4s)\,^1P_1$ level, at 11.63 and 11.83 eV above the ground state, respectively]. The latter

TABLE IV. Production and loss processes for the Ar_m^* atoms. Also given are the models where the rates are taken from, or the rate coefficients (if the rates are calculated in the fluid model itself), and the references of these data.

Production of Ar_m^* atoms		
Electron impact excitation from Ar atoms	$Ar^0 + e^- \rightarrow Ar_m^* + e^-$	From electron MC model
Ar^+/e^- radiative recombination	$Ar^+ + e^- \rightarrow Ar_m^* + h\nu$	$k = 10^{-11}\ cm^3\ s^{-1}$ (Ref. 47)
Loss of Ar_m^* atoms		
Electron impact ionization from Ar_m^*	$Ar_m^* + e^- \rightarrow Ar^+ + 2\ e^-$	From electron MC model
Electron impact excitation from Ar_m^*	$Ar_m^* + e^- \rightarrow Ar^{**} + e^-$	From electron MC model
Electron quenching of Ar_m^* (by excitation to the nearby resonant levels)	$Ar_m^* + e^- \rightarrow Ar_{res}^* + e^-$	$k = 1.6\times10^{-7}\ cm^3\ s^{-1}$ (Ref. 58)
Penning ionization of sputtered Cu atoms	$Ar_m^* + Cu^0 \rightarrow Ar^0 + Cu^+ + e^-$	$k = 1.4\times10^{-11} T_g^{1/2}\ cm^3\ s^{-1}$ (Ref. 10)
Two-body collisions with gas atoms, leading to deexcitation	$Ar_m^* + Ar \rightarrow Ar + Ar$	$k = 2.3\times10^{-15}\ cm^3\ s^{-1}$ (Ref. 54)
Three-body collisions with gas atoms, leading to Ar_2^*	$Ar_m^* + 2\ Ar \rightarrow Ar_2^* + Ar$	$k = 1.4\times10^{-32}\ cm^6\ s^{-1}$ (Ref. 54)
Collisions between two Ar_m^* atoms, followed by ionization of one of the atoms	$Ar_m^* + Ar_m^* \rightarrow Ar^+ + Ar^0 + e^-$	$k = 6.3\times10^{-10}\ cm^3\ s^{-1}$ (Ref. 59)
Collisions between two Ar_m^* atoms, followed by associative ionization	$Ar_m^* + Ar_m^* \rightarrow Ar_2^+ + e^-$	$k = 5.7\times10^{-10}\ cm^3\ s^{-1}$ (Ref. 59)

process, also called ''electron quenching'' does not require a high energy, and can therefore be induced again by slow electrons. Hence, it is treated in the fluid model itself, using a rate coefficient and the slow electron density.

Again, collisions between two Ar_m^* atoms can lead either to ionization of one of the atoms or to associative ionization. From the rate coefficients of both processes (see Table IV), it can be deduced that the ratio of formation of Ar^+ and Ar_2^+ ions is 0.525/0.475.

E. Monte Carlo model for He^+ ions

The He^+ ions are not only described with a fluid model (see above), but also with a MC model. Both models are, in fact, complementary. Indeed, the fluid model calculates the density with a continuity equation, coupled to Poisson's equation, to obtain a self-consistent electric field distribution, whereas the MC model uses this electric field distribution as input data. It provides a microscopic picture of the ion behavior (detailed trajectory and occurrence of collisions) and calculates the ion energy distribution (e.g., needed to calculate the sputtering rate). It is, however, verified that both models calculate the same values for the ion density and flux.

The principles of this ion MC model are similar to those of the electron MC model: the ion trajectory is calculated with Newton's laws, and the collisions (occurrence of a collision, kind of collision, and new energy and direction after collision) are treated with random numbers. The collisions taken into account in this model are elastic collisions with He atoms (both with isotropic scattering and with backward scattering, to simulate symmetric charge transfer[60]) and elastic collisions with Ar atoms. The cross sections of these processes are adopted from Ref. 26, and are plotted as a function of He^+ ion energy in Fig. 2(a).

F. Monte Carlo model for Ar^+ ions

A similar MC model is also applied to the Ar^+ ions. The collisions taken into account in this model, include elastic collisions with Ar atoms (again, both with isotropic scattering and with backward scattering, to simulate symmetric charge transfer[60]) and elastic collisions with He atoms. The cross sections[26,60] of these processes are plotted as a function of Ar^+ ion energy in Fig. 2(b).

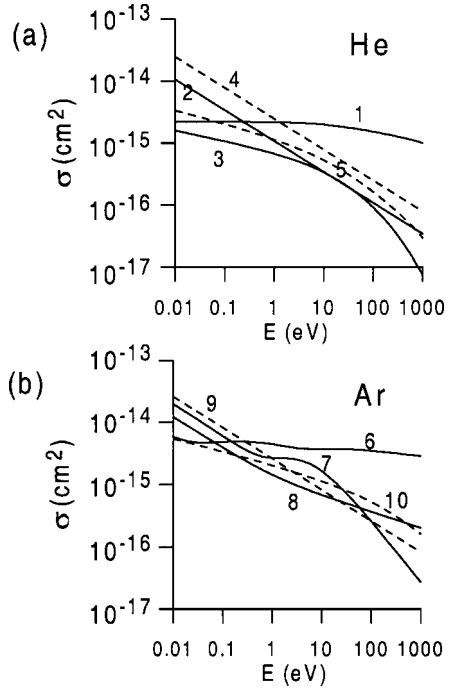

FIG. 2. Cross sections of (a) the He^+ ions and fast He atoms, and (b) the Ar^+ ions and fast Ar atoms, as a function of ion or atom energy. The solid lines represent the reactions with alike species (He/He and Ar/Ar), whereas the dashed lines stand for the crossed reactions (He/Ar and Ar/He). (1) elastic scattering in backward direction of He^+ ions with He (to simulate symmetric charge transfer), (2) elastic isotropic scattering of He^+ ions with He (see Ref. 26), (3) elastic scattering of He atoms with He (see Ref. 26), (4) elastic scattering of He^+ ions with Ar (see Ref. 26), (5) elastic scattering of He atoms with Ar (see Ref. 26), (6) elastic scattering in backward direction of Ar^+ ions with Ar (see Ref. 60) (to simulate symmetric charge transfer), (7) elastic isotropic scattering of Ar^+ ions with Ar (see Ref. 60), (8) elastic scattering of Ar atoms with Ar (see Ref. 60), (9) elastic scattering of Ar^+ ions with He (see Ref. 26), and (10) elastic scattering of Ar atoms with He (see Ref. 26).

G. Monte Carlo model for fast He atoms and fast Ar atoms

He^+ and Ar^+ ions can create fast He and Ar atoms by elastic collisions with He and Ar gas atoms. These fast He and Ar atoms are also followed with a MC model on their way toward the cathode, because they might play a non-negligible role in cathode sputtering due to their high flux bombarding the cathode.[23] The principle is again the same as for the other MC models. The collisions taken into account, for both fast He and Ar atoms, are elastic collisions with both He and Ar gas atoms. The cross sections[26,60] of these processes are illustrated in Figs. 2(a) and 2(b) (for He and Ar atoms, respectively).

H. Sputtering of Cu cathode

Based on the flux energy distributions of the He^+ ions, Ar^+ ions, fast He and fast Ar atoms, and Cu^+ ions (see below) calculated in the MC models, multiplied with the corresponding sputtering yields as a function of bombarding energy, the flux of sputtered Cu atoms at the cathode is computed:

$$J_{\text{sput}} = -\int_E \lfloor Y_{\text{He-Cu}}(E)*(F_{\text{He}^+}(E)+F_{\text{He}}(E)) + Y_{\text{Ar-Cu}}(E)*(F_{\text{Ar}^+}(E)+F_{\text{Ar}}(E)) + Y_{\text{Cu-Cu}}(E)*F_{\text{Cu}^+}(E)\rfloor dE.$$

Here, $Y(E)$ and $F(E)$ stand for the various sputtering yields and flux energy distributions, respectively. The sputtering yields as a function of bombarding energy are calculated with an empirical formula for perpendicular bombardment.[61] This is a reasonable assumption because the ions are directed by the electric field in the forward direction. The atoms are formed from the ions, and although they are subject to scattering collisions, they still move relatively in the forward direction. The minus sign indicates that the flux of sputtered Cu atoms is in the opposite direction of the fluxes of the bombarding particles. This formula is used for the entire cathode area.

I. Monte Carlo model for thermalization of sputtered Cu atoms

When the Cu atoms are sputtered from the cathode, they have typical energies of a few eV.[62] They lose this energy, however, rapidly by elastic collisions with He and Ar gas atoms until they are thermalized. This thermalization process is described with a MC model, in analogy to the MC models described above. More information can be found in Ref. 63. The output of this MC model is the so-called thermalization profile, i.e., the number of thermalized atoms as a function of distance from the cathode, which is used as input in the next model (see below).

J. Fluid model for thermalized Cu atoms and Cu^+ ions

Once the sputtered Cu atoms are thermalized, their transport is diffusion dominated. The behavior of the thermalized Cu atoms is described with a fluid model, consisting of a continuity equation and a transport equation (based on diffusion). This fluid model also describes the behavior of Cu^+ ions, which is coupled to the behavior of Cu atoms by various ionization mechanisms. This yields two coupled continuity equations and transport equations:

$$\frac{\partial n_{\text{Cu}}}{\partial t} + \overline{\nabla \cdot j_{\text{Cu}}} = R_{\text{prod,Cu}} - R_{\text{loss,Cu}},$$

$$\overline{j_{\text{Cu}}} = -D_{\text{Cu}} \overline{\nabla} n_{\text{Cu}},$$

$$\frac{\partial n_{\text{Cu}^+}}{\partial t} + \overline{\nabla} \cdot \overline{j_{\text{Cu}^+}} = R_{\text{prod,Cu}^+},$$

$$\overline{j_{\text{Cu}^+}} = \mu_{\text{Cu}^+} n_{\text{Cu}^+} \overline{E} - D_{\text{Cu}^+} \overline{\nabla} n_{\text{Cu}^+}.$$

The various symbols have been explained above. The transport coefficients of Cu atoms and Cu^+ ions in the He/Ar gas mixture are again calculated from the values in the pure gases by Blanc's law (see above). The diffusion coefficients in the pure gases are again determined from rigid sphere theory,[36] and the mobility of Cu^+ ions in pure He and pure Ar is adopted from Ref. 34.

The production rate of Cu atoms is given by the sputtering flux, multiplied with the thermalization profile (see above). The loss rate of Cu atoms is equal to the production rate of Cu^+ ions, and is determined by various ionization mechanisms, i.e., electron impact ionization, Penning ionization by He_m* and by Ar_m* atoms, and asymmetric charge transfer by He^+ and Ar^+ ions. The rate of electron impact ionization is calculated in the electron MC model. The rates of Penning ionization and asymmetric charge transfer are calculated in the present fluid model, based on the density of Cu atoms (calculated in this model), multiplied with the densities of He_m*, Ar_m*, He^+, and Ar^+ (calculated in the corresponding models, see above) and with the corresponding rate coefficients of Penning ionization and asymmetric charge transfer (values given in Tables II, III, and IV). No specific loss mechanism is taken into account for the Cu^+ ions, except from recombination at the cell walls (which is determined by the boundary conditions).

K. Monte Carlo model for Cu^+ ions

Finally, a MC model is applied for the Cu^+ ions, in analogy to the MC models for He^+ and Ar^+ ions. Indeed, this MC model allows us to calculate, in analogy to the He^+ and Ar^+ MC models, the flux energy distribution of the Cu^+ ions bombarding the cathode, which is used to calculate the sputtering flux (see above). Indeed, as will be shown below, Cu^+ ions play a non-negligible role in the sputtering process (so-called ''self-sputtering'').

L. Coupling of the models

All the models described above are coupled to each other due to the interaction processes between the different species. Hence, they are solved iteratively until final convergence is reached.

Initially, the *electron MC model* is run, assuming a certain electric field distribution (i.e., linearly decreasing in the CDS, and zero in the NG) and ion fluxes bombarding the cathode (based on the macroscopic electrical current). Output of this model are the various ionization and excitation rates (of He and Ar gas atoms, He_m* and Ar_m* metastable atoms, and Cu atoms) and the slow electron transfer rate.

The ionization rates of He and Ar, i.e., the production rates of He^+ and Ar^+ ions, and the slow electron transfer rate, are used as input in the *fluid model for slow electrons and ions*. For the other input data of this fluid model, e.g., other production rates of the ions (which are calculated in the other models; see Table II), we have simply assumed some constant values for this first iteration. The output of this fluid model includes the electric field distribution and the ion fluxes bombarding the cathode (both needed for the electron MC model), as well as the densities of the slow electrons and the various ions.

Next, the two *fluid models for the* He_m* *and* Ar_m* *metastable atoms* are calculated, using the input from the electron MC model and the electron–ion fluid model. Output of the metastable models are the densities of the He_m* and Ar_m* metastable atoms, as well as some rates of production and loss processes for the other plasma species (see Tables II, III, and IV).

Subsequently, the *MC models for* He^+ *ions,* Ar^+ *ions,* and *fast He and Ar atoms* are run, using the electric field distribution from the electron–ion fluid model. The most important output data of these MC models are the ion and fast atom flux energy distributions at the cathode, which are needed to calculate the sputtering flux.

When the latter is calculated, the *thermalization of the sputtered Cu atoms* is simulated with the *MC model*. The output is the thermalization profile (see above), which is used, together with the sputtering flux, as the input production rate in the fluid model for Cu atoms and Cu^+ ions.

The other input for the Cu/Cu^+ *fluid model* includes the electron impact ionization rate (from the electron MC model), as well as the densities of He and Ar metastable atoms (calculated from the corresponding metastable fluid models) and of He^+ and Ar^+ ions (adopted from the electron–ion fluid model), which are used to calculate the rates of Penning ionization and of asymmetric charge transfer, respectively. Output data of this fluid model are the densities of Cu atoms and Cu^+ ions, and the ionization rate of Cu, i.e., the production rate of Cu^+ ions.

Finally, the Cu^+ MC model is run, using the above production rate of Cu^+ ions. This model yields as the most important output the Cu^+ ion flux energy distribution at the cathode, needed to calculate the sputtering flux in the second iteration.

When all models have been calculated once, the procedure is repeated, i.e., all models are calculated again, with updated information of production and loss rates, electric field distribution, etc. as input data. Typically, 3–4 iterations are needed before convergence is reached. While some models take only a few minutes to reach convergence (e.g., the metastable fluid models, and the Cu/Cu^+ fluid model), other models take a much longer time, such as the MC models (which typically take a few hours, depending on statistics), and especially the electron–ion fluid model. Indeed, in the latter model, a small time step has to be used to avoid numerical instabilities in solving the coupled differential equations. Hence, this model typically takes 5–10 h on today's fast computers to reach convergence. Therefore, the entire modeling network takes a few days before final convergence is reached.

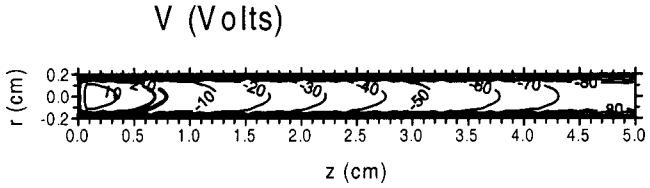

FIG. 3. Calculated two-dimensional potential distribution, at 388 V, 2 A, 17 Torr, and 5% Ar addition. The upper and lower borders of the figure are the cathode cylinder walls (sidewall), and the left and right border represent the open ends of the tube. The anode ring is at the left, whereas at the right-hand side another HCD is assumed.

III. RESULTS AND DISCUSSION

The HCD used in the model has a length of 5 cm and an inner diameter of 4 mm. It is assumed to be open at both sides. At one side, there is an anode ring. At the other side, there is again a HCD. This construction is typical for laser applications, i.e., a repetition of a few HCD tubes increases the laser output power.[64] The distance between the HCD and anode ring is assumed to be 0.3 mm, so that no discharge is formed in between the HCD and anode. At the other side, reflecting boundary conditions are applied.

All calculation results will be presented for a discharge voltage and current of 388 V and 2 A, respectively, and a gas pressure of 17 Torr, in a ratio of 95% He and 5% Ar. These are experimental operating conditions for the present discharge geometry.[64]

A. Potential distribution

Figure 3 shows the calculated two-dimensional potential distribution. The potential is equal to −388 V at the cathode sidewalls, and rises rapidly as a function of distance away from the cathode, in the first millimeter adjacent to the cathode. This region is the cathode dark space. The electric field near the cathode sidewalls is in the order of 20–40 kV/cm. More toward the center of the discharge tube, i.e., in the negative glow, the potential still changes considerably in the radial direction, giving rise to radial electric field values ranging between 10 and 50 V/cm. Also, in the axial direction, the potential changes significantly, from slightly positive values (at maximum 10 V) near the anode side ($z=0$ -0.3 cm) to −75 V at $z=5$ cm, giving rise to axial electric field values of about 20 V/cm. Hence, although the discharge geometry (i.e., a very long and narrow tube) would suggest that one-dimensional models (i.e., in the radial direction) would be sufficient, the axial nonuniformity of the potential distribution and of other plasma characteristics (see below and, also, Refs. 65,66) clearly show that the models should really be developed in at least two dimensions.[67]

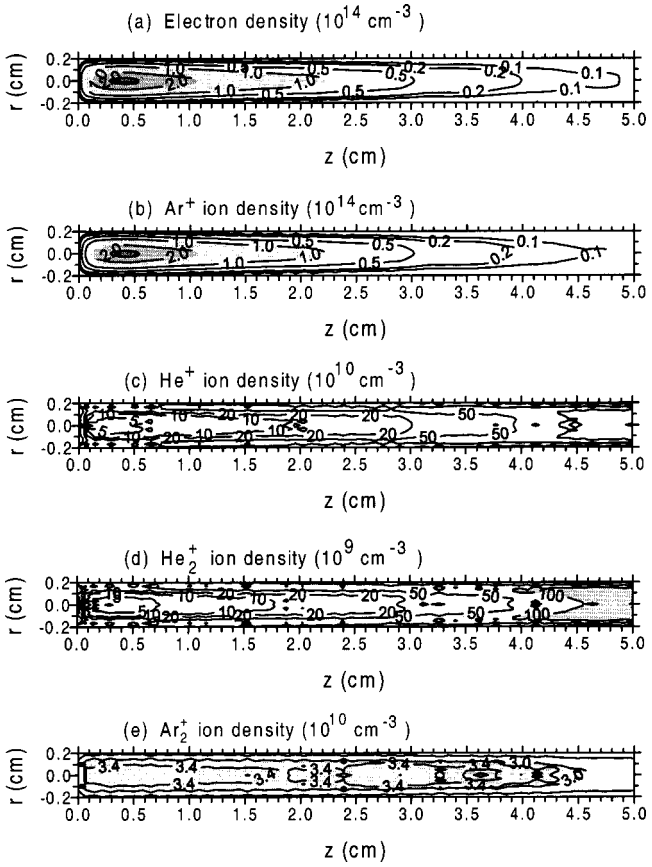

FIG. 4. Calculated two-dimensional density profiles of the electrons (a), Ar^+ ions (b), He^+ ions (c), He_2^+ ions (d), and Ar_2^+ ions (e), at the same operating conditions as in Fig. 3.

The significant potential drop in the NG in the axial direction results in a considerable axial electric field in the entire discharge tube. The latter gives rise to an electron current in the longitudinal direction, toward the anode, which is responsible for the conduction of the electrical current. This longitudinal electron current is mostly due to slow electrons. The fast electrons, on the other hand, move primarily in the transverse direction, i.e., perpendicular to the cathode surface, and they give rise to various collisions, yielding excitation and ionization of the gas atoms.[67]

It appears from Fig. 3 that the potential in the NG, i.e., the so-called plasma potential, is negative in most of the discharge tube. This is in contrast to planar cathode glow discharges, where the plasma potential is typically positive (see, e.g., Ref. 24). However, the fact that the plasma potential can be negative in HCDs has also been experimentally demonstrated.[68,69] Indeed, there is no need for the plasma potential to become positive in order to guarantee the discharge current balance, as is the case in planar cathode glow discharges, because the special geometry of the HCD reduces the loss of fast electrons to the anode, and it allows a sufficiently high ion flux toward the cathode.

B. Plasma species densities

Figure 4 presents the calculated two-dimensional density profiles of the electrons (a), and Ar^+ (b), He^+ (c), He_2^+ (d), and Ar_2^+ (e) ions. The electron density reaches a maximum of $2.5\times10^{14}\,\mathrm{cm}^{-3}$ at the tube axis and at $z=0.4$ cm, i.e., near the anode side, and it drops over more than an order of magnitude in the axial direction, towards the other end of the discharge tube. Hence, the electron density profile is also strongly nonuniform in the axial direction. The reason for this asymmetric density profile is found in the potential distribution (Fig. 3), which shows the highest (i.e., most positive) plasma potential near the anode side, at $z=0-0.3$ cm. This gives rise to the highest radial electric field values in this region. Hence, the electrons can gain most of their energy here. In combination with the flux of secondary electrons emitted from the cathode, which is at maximum around $z=0.3-0.5$ cm, it is expected that most electron impact ionization (and excitation) takes place in this region, leading to the highest production of electrons, and hence a maximum in the electron density.

This axial nonuniformity, which is also found back in other plasma quantities (see below) and has also experimentally been demonstrated,[65,66] is an important outcome of the model, because it can help to determine the proper cathode length for the longitudinal HCD He–Cu^+ ion laser. Indeed, when the HCD length exceeds a certain value, increasing the length will probably not result in a higher discharge efficiency, and hence in a higher laser output power, because the plasma species densities, excitation and ionization rates, etc., have dropped to very low values at a large distance from the anode ring. It might, therefore, be more efficient when the laser active volume comprises a series of hollow anodes and cathodes, in which each cathode has a length of about 1–2 cm.

The Ar^+ ion density distribution [Fig. 4(b)] is roughly the same as the electron density profile, which shows that the Ar^+ ions are the dominant ionic species at the discharge conditions under study. Indeed, He^+ ions are characterized by a very low density, as is clear from Fig. 4(c). The maximum He^+ ion density is in the order of a few times $10^{12}\,\mathrm{cm}^{-3}$, and is reached at both side ends of the discharge tube, where the electron density is low. At the position where the electron density has its maximum value, the He^+ ion density shows a local dip of $5\times10^{10}\,\mathrm{cm}^{-3}$. The reason for this opposite density profile of He^+ ions compared to electrons is because He^+ ions are easily lost by recombination with two electrons (see Table II, and also Table V). Indeed, as appears from Table II, the rate coefficient of this process is several orders of magnitude higher than the corresponding rate coefficient for Ar^+ ions, which explains why Ar^+ ions are the dominant ionic species at the conditions under study, in spite of the fact that the Ar gas constitutes only 5% of the total gas mixture. This very low He^+ ion density might explain the experimentally observed saturation of the laser power with increasing current, at high electrical currents, in He–Cu IR lasers.[7,11,70] Indeed, the laser power is proportional to the Cu^+ upper laser level, which is populated by asymmetric charge transfer of Cu atoms with He^+ ions. In normal circumstances, the density of charged species (ions and electrons) increases with current; hence, a higher current gives a higher He^+ ion density, and consequently, a higher laser power. However, when the electron density increases above a certain value, recombination with two electrons be-

TABLE V. Calculated relative contributions of the most important production and loss mechanisms of the various plasma species

Species	Production processes (%)	Loss processes (%)
Electrons	Electron impact ionization of He (47)	Recombination with He^+ (75)
	Electron impact ionization of Ar (45)	Recombination with Ar^+ (2.6)
	Penning ionization of Ar by He_m* (5)	Recombination with He_2^+ (5)
	Hornbeck–Molnar associative ionization of He(3)	Recombination with Ar_2^+ (1.4)
		Diffusion+recombination at walls (16)
He^+ ions	Electron impact ionization of He (100)	Recombination with electrons (81)
		Diffusion+recombination at walls (18)
		Asymmetric charge transfer with Cu (1)
Ar^+ ions	Electron impact ionization of Ar (89)	Diffusion+recombination at walls (82)
	Penning ionization of Ar by He_m* (11)	Asymmetric charge transfer with Cu (11)
		Recombination with electrons (4)
		Conversion into Ar_2^+ ions (3)
He_2^+ ions	Hornbeck–Molnar associative ionization (98)	Recombination with electrons (85)
	Metastable–metastable associative ionization (1)	Diffusion+recombination at walls (15)
	Conversion from He^+ ions (1)	
Ar_2^+ ions	Conversion from Ar^+ ions (98)	Recombination with electrons (96)
	Hornbeck–Molnar associative ionization (1)	Diffusion+recombination at walls (4)
	Metastable-metastable associative ionization (1)	
He_m* atoms	Electron impact excitation of He (16)	Electron impact ionization from He_m* (80)
	He^+–electron recombination (82)	Penning ionization of Ar (13)
	He_2^+–electron recombination (2)	Penning ionization of Cu (2)
		Electron impact deexcitation (1)
		Diffusion+deexcitation at walls (4)
Ar_m* atoms	Electron impact excitation of Ar (100)	Electron impact excitation from Ar_m* (91)
		Electron impact ionization from Ar_m* (1)
		Electron quenching to resonant levels (7)
Cu atoms	Sputtering by Ar^+ ions (56)	Electron impact ionization (76)
	Sputtering by fast Ar atoms (26)	Asymmetric charge transfer with Ar^+ ions (17)
	Sputtering by Cu^+ ions (16)	Asymmetric charge transfer with He^+ ions (1.7)
	Sputtering by He^+ ions (0.5)	Penning ionization by Ar_m* atoms (0.3)
	Sputtering by fast He atoms (1.5)	Penning ionization by He_m* atoms (5)
Cu^+ ions	Electron impact ionization (76)	Diffusion+recombination at walls (100)
	Asymmetric charge transfer with Ar^+ ions (17)	
	Asymmetric charge transfer with He^+ ions (1.7)	
	Penning ionization by Ar_m* atoms (0.3)	
	Penning ionization by He_m* atoms (5)	

comes so important that it causes saturation in the He^+ ion density with further increase of the current, which then results in saturation of the laser power.

The high electron density does not only give rise to a low He^+ ion density, but also to rather low He_2^+ and Ar_2^+ ion densities. Indeed, both molecular ions are also easily lost by recombination with electrons (see Table V). He_2^+ ions [Fig. 4(d)] are characterized by a similar density profile as He^+ ions, with a maximum of almost $10^{12}\,cm^{-3}$ at both side ends of the discharge tube, and a dip of $2\times10^9\,cm^{-3}$ at $z=3$ mm, i.e., where the electron density reaches its maximum. The Ar_2^+ ion density is more uniformly distributed in the discharge tube, as is clear from Fig. 4(e), with overall values of about $3.4\times10^{10}\,cm^{-3}$, and a maximum of a few times $10^{11}\,cm^{-3}$ near the side end of the tube.

The two-dimensional density profiles of the He_m* and Ar_m* metastable atoms are presented in Figs. 5(a) and 5(b). Figures 5(a) and 5(b) do not show very smooth profiles, due to statistical limitations. Indeed, some of the major production and loss mechanisms of metastable atoms, i.e., electron impact excitation to the metastable level, and ionization and (de)-excitation from the metastable level, do not occur with high probability, and a large number of electrons has to be followed in the electron MC model before the rates of these processes show reasonable values. In fact, we have followed the electrons for several weeks on a professional workstation with alpha processor (EV67), and the statistics are still not yet satisfactory to produce smooth density profiles, as appears from Figs. 5(a) and 5(b). Nevertheless, it can be de-

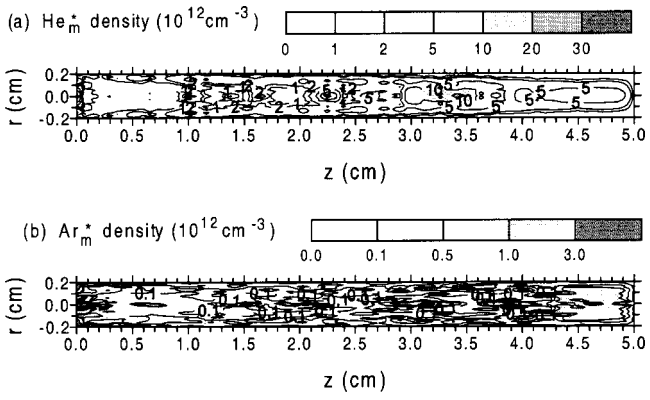

FIG. 5. Calculated two-dimensional density profiles of the He_m* (a) and Ar_m* (b) metastable atoms, at the same operating conditions as in Fig. 3.

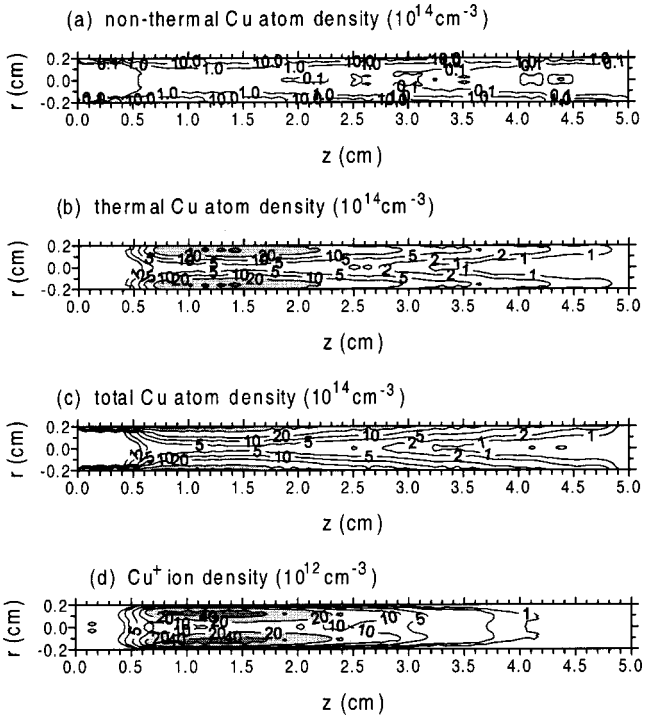

FIG. 6. Calculated two-dimensional density profiles of the nonthermal Cu atoms (a), the thermal Cu atoms (b), the total Cu atom population (sum of thermal and nonthermal atoms) (c), and Cu^+ ions (d), at the same operating conditions as in Fig. 3.

duced from Figs. 5(a) and 5(b) that both He_m* and Ar_m* metastable atoms reach a maximum near the open end of the HCD (at the anode side) and at a distance $z>2-3$ cm. Hence, the maximum of the metastable densities does not coincide with the maximum electron density [see Fig. 4(a)]. The overall He_m* and Ar_m* metastable densities in the discharge tube are found to be in the order of $1-5\times10^{12}$ and 10^{11} cm^{-3}, respectively. Hence, the He_m* density is calculated to be more than an order of magnitude higher than the Ar_m* density, which appears to be attributed to the efficient production by the He^+–electron recombination (see Table V).

Figure 6 illustrates the two-dimensional density profiles of the sputtered Cu atoms and Cu^+ ions. As mentioned above, when the Cu atoms are sputtered from the cathode, they have typical energies of a few eV, which they lose very rapidly by collisions with He and Ar gas atoms. Hence, the density of the nonthermal sputtered Cu atoms [Fig. 6(a)] is at a maximum ($\sim$order of 10^{16} cm^{-3}) at the cathode sidewalls, where the atoms are released by sputtering, and it drops very rapidly toward values of 10^{13} cm^{-3} at the tube axis. Once the Cu atoms are thermalized, their transport is diffusion dominated. Figure 6(b) presents the density profile of the thermal Cu atoms. It reaches a maximum of 4.5×10^{15} cm^{-3} very close to the cathode sidewalls, and drops also as a function of distance away from the cathode. At the tube axis, it reaches values around $2-5\times10^{14}$ cm^{-3}, as is apparent from Fig. 6(b). The total sputtered Cu atom density profile is shown in Fig. 6(c). By comparing Figs. 6(a)–6(c), it is clear that the thermal Cu atoms form the major contribution to the overall Cu atom density, and the nonthermal Cu atoms are only significant adjacent to the cathode sidewalls. Finally, the Cu^+ ion density profile is illustrated in Fig. 6(d). It reaches a maximum of about 5×10^{13} cm^{-3} around $z=1$ cm (i.e., where the Cu atoms reach their maximum density) and at $r=1$ mm, i.e., not at the tube axis. The reason is that the Cu^+ ions are mainly formed by electron impact ionization (see below), which is at maximum in this region. From the calculated Cu atom and Cu^+ ion densities, the overall ionization degree of Cu is computed to be about 1%.

C. Production and loss mechanisms of various plasma species

Table V presents the calculated relative contributions of the most important production and loss processes for the various plasma species.

The electrons are mainly formed by electron impact ionization of He and Ar gas atoms. Both processes appear to be of the same importance, which is a bit unexpected, because the He gas atom density is considerably higher than the Ar gas atom density (ratio of 95%–5%; see above). However, as was illustrated in Fig. 1(a), the cross section of the electron impact ionization of Ar is almost an order of magnitude higher than the corresponding value for He, and it reaches a maximum at a somewhat lower energy, which corresponds better to the typical electron energies at the conditions under study. Hence, this compensates for the lower Ar gas atom density, and results in a nearly equal occurrence of electron impact ionization of He and Ar gas atoms. Beside electron impact ionization, some other processes, listed in Table V, contribute a few %, while the other processes taken into account (see Table II) are not important.

As far as the loss of electrons is concerned, the electron–ion recombination with He^+ ions seems to be the most important, although recombination with Ar^+, He_2^+, and Ar_2^+ ions is also not negligible, with contributions of a few %. Finally, recombination at the walls of the discharge tube is also quite important, as appears from Table V.

He^+ and Ar^+ ions are dominantly formed by electron impact ionization of He and Ar gas atoms, respectively, although Penning ionization of Ar by He_m* metastable atoms is also quite important for the production of Ar^+ ions. Ionization by collisions of two He_m* or Ar_m* metastable atoms, on the other hand, is negligible for the production of He^+ and Ar^+ ions.

The loss of He^+ ions is mainly attributed to recombination with electrons, as was already stated above. Diffusion toward and subsequent recombination at the tube walls is also rather important. Asymmetric charge transfer with sputtered Cu atoms contributes only 1%, and conversion into He_2^+ ions is found to be negligible (0.03%). For the Ar^+ ions, a different behavior is seen. Indeed, the major loss mechanism appears to be diffusion to, and subsequent recombination at, the walls, whereas recombination in the plasma contributes only a few %. This was anticipated already above, based on the lower recombination rate coefficients (Table II) and the high calculated Ar^+ ion density [Fig. 4(b)]. On the other hand, asymmetric charge transfer with Cu atoms, and to a less extent also conversion into Ar_2^+ ions, appear not to be negligible as loss mechanisms.

The major production mechanisms for He_2^+ and Ar_2^+ ions also appear to be different. Indeed, He_2^+ ions are mainly formed by Hornbeck–Molnar associative ionization, whereas the dominant production process for Ar_2^+ ions seems to be conversion from Ar^+ ions. The reason is found in the much higher Ar^+ ion density compared to the He^+ ion density, making conversion from Ar^+ ions more important than from He^+ ions. The relative importance of the loss mechanisms, on the other hand, is found to be very similar for He_2^+ and Ar_2^+ ions, with a major contribution of the electron–ion recombination in the plasma, and a minor contribution of recombination at the walls of the discharge tube.

Also, for He_m* and Ar_m* metastable atoms, different processes appear to be the dominant production mechanisms. Ar_m* atoms are almost exclusively formed by electron impact excitation from the Ar ground state. This process also plays a role in He_m* atoms, but the major production mechanism for the latter species is recombination between He^+ ions and electrons, as appears from Table V. Indeed, the rate coefficient of this process is very high (see Table II), and this process is claimed to lead to 100% formation of He_m* atoms.[20] The importance of this process for the production of He_m* atoms explains why the density of the latter species is significantly higher than the Ar_m* density (see Fig. 5).

As far as the loss of these species is concerned, electron impact ionization from the He_m* metastable level is the most important loss mechanism for He_m* atoms, but diffusion and subsequent deexcitation at the walls, as well as Penning ionization of Ar atoms, and to a less extent of sputtered Cu atoms, also play a non-negligible role. Electron impact deexcitation, on the other hand, is only of minor importance. The other loss mechanisms taken into account in the He_m* model (see Table III) were found to be completely negligible. For Ar_m* atoms, electron impact excitation from the Ar_m* metastable level to higher levels, appears to be the dominant loss mechanism. Electron quenching to the nearby resonant levels, and electron impact ionization from the Ar_m* metastable level, also have a minor contribution, but the other loss mechanisms considered in this model are calculated to be negligible.

Finally, Cu atoms are produced by sputtering in our model. It appears from Table V that the Ar^+ ions play a dominant role in sputtering, in spite of the fact that the Ar gas constitutes only 5% of the gas mixture. This model result confirms that the addition of Ar to the He gas is really beneficial to promote sputtering of the Cu cathode because He^+ ions are not very efficient for sputtering due to their low mass. Beside Ar^+ ions, fast Ar atoms created in collisions from Ar^+ ions, are also important for sputtering. Indeed, although they are characterized by lower energy, because they cannot gain energy from the electric field in the CDS, their flux toward the cathode is considerable, which explains their large contribution to sputtering. Also, Cu^+ ions play quite an important role in sputtering (i.e., self-sputtering), which is mainly attributed to their high energy when bombarding the cathode.[71] He^+ ions and fast He atoms, on the other hand, have only a minor contribution to sputtering, as is expected because of their low mass.

The loss of Cu atoms is due to ionization, and hence, this is equal to the production of Cu^+ ions. From the various ionization mechanisms incorporated in the model, electron impact ionization appears to be the most important. Further, asymmetric charge transfer of Cu atoms with Ar^+ ions is also quite important, which is attributed to the high calculated Ar^+ ion density, in comparison to, for example, the He^+ ion density (see Fig. 4). Indeed, the contribution of asymmetric charge transfer by He^+ ions is calculated to be only 5%. The latter process is, however, responsible for populating the Cu^+ upper laser level of the 780.8 nm laser line, and hence the rate of this process determines the laser power. It appears that the laser power is limited by the rather low He^+ ion density, which is the result of electron–ion recombination at high electron densities, typical for high electrical currents. This can maybe explain the saturation in laser power, which is often observed in He–Cu lasers.[7,11,70] Further, beside electron impact ionization and asymmetric charge transfer, Penning ionization of Cu by Ar_m*, and especially by He_m* metastable atoms (because of their higher density), also plays a non-negligible role in the ionization of Cu atoms, and hence in the production of Cu^+ ions.

Finally, the loss of Cu^+ ions is solely attributed in our model to diffusion and subsequent recombination at the walls of the discharge tube.

IV. CONCLUSION

A modeling network is developed for a Cu HCD in a He/Ar gas mixture, typical for laser applications. The species considered in the model are He and Ar gas atoms; electrons; He^+, Ar^+, He_2^+, and Ar_2^+ ions; fast He and Ar atoms; He_m* and Ar_m* metastable atoms; and sputtered Cu atoms and the Cu^+ ions. These species are described with a combination of Monte Carlo models and fluid models. All these models are coupled to each other due to the interaction processes between the species, and they are solved iteratively until final convergence is reached.

The results of the modeling network include the electric potential distribution, the plasma species densities, and the relative contributions of production and loss mechanisms of the various plasma species. These results are presented for a longitudinal HCD at typical laser conditions, i.e., 388 V, 2 A, 17 Torr, 95% He, and 5% Ar.

The electric potential distribution shows a narrow CDS in front of the cathode sidewalls. In the NG, the potential is severely nonuniform in the axial direction, resulting in a rather strong axial electric field. The latter gives rise to a considerable electron flux toward the anode, which is necessary to conduct the electrical current. Moreover, the plasma potential in the NG is calculated to be negative in most of the discharge tube, which is in contrast to planar cathode glow discharges, but has been observed also experimentally in HCDs.

The calculated electron density is also strongly nonuniform in the axial direction, with a maximum of $2.5 \times 10^{14}\,cm^{-3}$ around $z = 0.4$ cm, attributed to the highest radial electric field in this region, and hence the highest electron energy and most efficient electron impact ionization.

Ar^+ ions are found to be the dominant ionic species, and they are characterized by the same density profile as the electrons. The densities of He^+, $He_2{}^+$, and $Ar_2{}^+$ ions, on the other hand, are found to be rather small ($\sim 10^{10} - 10^{11}\,cm^{-3}$), due to efficient recombination with electrons. They typically reach a dip where the electron density has its maximum, except for the $Ar_2{}^+$ ions, which are more uniformly distributed in the plasma. The He_m* and Ar_m* metastable densities are calculated in the order of $1-5\times10^{12}$ and $10^{11}\,cm^{-3}$, respectively, in most of the discharge tube. The sputtered Cu atom density reaches a maximum of almost $2\times10^{16}\,cm^{-3}$ near the cathode sidewalls, and it drops to values of $1-5\times10^{14}\,cm^{-3}$ at the tube axis. The thermal Cu atoms constitute the major fraction of Cu atoms, except close to the cathode sidewalls. Finally, the Cu^+ ion density reaches a maximum of $5\times10^{13}\,cm^{-3}$ at 1 mm from the cathode sidewalls, i.e., not at the tube axis. The ionization degree of Cu is calculated to be about 1%.

Finally, the relative contributions of the various production and loss mechanisms of the plasma species are calculated. Electron impact ionization appears to be the dominant production mechanism for the electrons and He^+ and Ar^+ ions, whereas $He_2{}^+$ and $Ar_2{}^+$ ions are mainly formed by Hornbeck–Molnar associative ionization (for $He_2{}^+$) and by conversion from Ar^+ ions (for $Ar_2{}^+$). The major loss mechanisms of the electrons and ionic species are recombination in the plasma and at the tube walls. He_m* metastable atoms are mainly created by recombination between He^+ ions and electrons, and to a less extent by electron impact excitation from the ground-state atoms. The latter process is, however, clearly the dominant production mechanism for Ar_m* metastable atoms. Electron impact ionization and excitation from the He_m* and Ar_m* metastable levels are found to be the dominant loss processes for these species. Sputtering by Ar^+ ions is the dominant production mechanism for the sputtered Cu atoms. The loss of Cu atoms is equal to the production of Cu^+ ions, and is attributed to various ionization mechanisms, of which electron impact ionization is calculated to be the most important. Asymmetric charge transfer with He^+ ions appears to contribute to only a few %, which is attributed to the low He^+ ion density. The latter process is responsible for populating the Cu^+ upper laser level of the 780.8 nm laser line. Hence, it is expected that the laser power is limited due to the rather low He^+ ion density, calculated for the discharge conditions under study. This might explain the experimentally observed saturation of He–Cu IR lasers at high electrical currents.

The different modeling results presented here give us a better insight into the HCD behavior, which is useful for optimization of laser operation. The model can be used to make predictions for the optimum cathode length (based on the axial nonuniformity), the optimum Ar addition to the He gas (for Cu sputtering), and the operating conditions resulting in optimum laser output power. We plan to report the result of these investigations in the near future.

ACKNOWLEDGMENTS

One of the authors (A. B.) is indebted to the Flemish Fund for Scientific Research (FWO) for financial support. This research is also sponsored by NATO's Scientific Affairs Division in the framework of the Science for Peace Program, and by the Federal Services for Scientific, Cultural, and Technical Affairs of the Prime Minister's Office through IUAP-V. Finally, the authors would like to thank M. Grozeva for providing the experimental setup and operating conditions and other helpful information, as well as Z. Donko and G. Bánó for the interesting discussions.

[1] D. C. Gerstenberger, R. Solanki, and G. J. Collins, IEEE J. Quantum Electron. **QE-16**, 820 (1980).
[2] I. G. Ivanov, E. L. Latush, and M. F. Sem, *Metal Vapor Ion Lasers: Kinetic Processes and Gas Discharges* Wiley, (Chichester, U.K., 1996).
[3] P. J. Slevin and W. W. Harrison, Appl. Spectrosc. Rev. **10**, 201 (1975).
[4] S. Caroli, Prog. Anal. At. Spectrosc. **6**, 253 (1983).
[5] A. Goldamn and J. Amoroux, *Gases: Macroscopic Processes and Discharges* (Plenum, New York, 1983).
[6] L. Csillag, M. Janossy, K. Rozsa, and T. Salamon, Phys. Lett. **50A**, 13 (1974).
[7] H. J. Eichler, H. J. Koch, J. Salk, and G. Schäfer, IEEE J. Quantum Electron. **QE-15**, 908 (1979).
[8] J. R. McNeil, G. J. Collins, K. B. Persson, and D. L. Franzen, Appl. Phys. Lett. **27**, 595 (1975).
[9] K. A. Peard, Z. Donko, K. Rozsa, L. Szalai, and R. C. Tobin, IEEE J. Quantum Electron. **QE-30**, 2157 (1994).
[10] R. R. Arslanbekov, R. C. Tobin, and A. A. Kudryatsev, J. Appl. Phys. **81**, 554 (1997).
[11] K. A. Peard, K. Rozsa, and R. C. Tobin, J. Phys. D **27**, 219 (1994).
[12] H. J. Eichler and W. Wittwer, J. Appl. Phys. **51**, 80 (1980).
[13] E. M. van Veldhuizen and F. J. de Hoog, J. Phys. D **17**, 953 (1984).
[14] B. E. Warner, K. B. Persson, and G. J. Collins, J. Appl. Phys. **50**, 5694 (1979).
[15] A. J. Lichtenberg and M. A. Lieberman, J. Appl. Phys. **87**, 7191 (2000).
[16] H. Koch and H. J. Eichler, J. Appl. Phys. **54**, 4939 (1983).
[17] J. Hamisch and J. de la Rosa, Appl. Phys. B: Photophys. Laser Chem. **43**, 189 (1987).
[18] G. J. Fetzer and J. J. Rocca, IEEE J. Quantum Electron. **QE-28**, 1941 (1992).
[19] G. Bánó, L. Szalai, P. Horváth, K. Kutasi, Z. Donkó, K. Rózsa, and T. M. Adamowicz, J. Appl. Phys. (in press).
[20] R. Deloche, P. Monchicourt, M. Cheret, and F. Lambert, Phys. Rev. A **13**, 1140 (1976).
[21] K. Kutasi, P. Hartmann, and Z. Donko, J. Phys. D **34**, 3368 (2001).
[22] Y. Ichikawa and S. Teii, J. Phys. D **13**, 2031 (1980).
[23] A. Bogaerts, M. van Straaten, and R. Gijbels, Spectrochim. Acta, Part B **50**, 179 (1995).
[24] A. Bogaerts, R. Gijbels, and W. J. Goedheer, J. Appl. Phys. **78**, 2233 (1995).
[25] T. Kato and R. K. Janev, *Atomic and Plasma-Material Interaction Data for Fusion*, Vol. 3 (International Atomic Energy Agency, Vienna, 1992), Vol. 3, p. 33.
[26] A. V. Phelps (private communication); ftp://jila.colorado.edu/collision_data
[27] F. J. de Heer and R. H. J. Jansen, J. Phys. B **10**, 3741 (1977).
[28] A. V. Phelps and Z. Lj. Petrovic, Plasma Sources Sci. Technol. **8**, R21 (1999).
[29] H. A. Hyman, Phys. Rev. A **20**, 855 (1979).
[30] H. A. Hyman, Phys. Rev. A **18**, 441 (1978).
[31] L. Vriens, Phys. Lett. **8**, 260 (1964).
[32] N. J. Mason and W. R. Newell, J. Phys. B **20**, 1357 (1987).
[33] J. D. P. Passchier and W. J. Goedheer, J. Appl. Phys. **74**, 3744 (1993).
[34] E. W. McDaniel, *Collision Phenomena in Ionized Gases* (Wiley, New York, 1964).
[35] H. W. Ellis, R. Y. Pai, E. W. McDaniel, E. A. Mason, and L. A. Viehland, At. Data Nucl. Data Tables **17**, 177 (1976).
[36] J. O. Hirschfelder, C. F. Curtiss, and R. B. Bird, *Molecular Theory of Gases and Liquids* (Wiley, New York, 1964).
[37] A. Bogaerts and R. Gijbels, J. Appl. Phys. **86**, 4124 (1999).
[38] D. L. Scharfetter and H. K. Gummel, IEEE Trans. Electron Devices **16**, 64 (1969).
[39] R. E. Huffmann and D. H. Katayama, J. Chem. Phys. **45**, 138 (1966).
[40] H. F. Wellenstein and W. W. Robertson, J. Chem. Phys. **56**, 1077 (1972).

[41] A. Bogaerts, R. Gijbels, and J. Vlcek, J. Appl. Phys. **84**, 121 (1998).
[42] W. L. Morgan, J. P. Boeuf, and L. C. Pitchford, Siglo Data Base, CPAT and Kinema Software (1998); http://www.csn.net/siglo
[43] G. D. Alkhazov, Sov. Phys. Tech. Phys. **15**, 66 (1970).
[44] C. B. Collins, B. W. Johnson, and M. J. Shaw, J. Chem. Phys. **57**, 5310 (1972).
[45] V. S. Vorob'ev, Plasma Sources Sci. Technol. **4**, 163 (1995).
[46] H. S. W. Massey and E. H. S. Burhop, *Electronic and Ionic Impact Phenomena* (Oxford University Press, Oxford, U.K., 1952).
[47] M. A. Biondi, Phys. Rev. **129**, 1181 (1963).
[48] F. J. Mehr and M. A. Biondi, Phys. Rev. A **16**, 322 (1968).
[49] R. Johnsen, A. Chen, and M. A. Biondi, J. Chem. Phys. **73**, 1717 (1980).
[50] E. A. Den Hartog, D. A. Doughty, and J. E. Lawler, Phys. Rev. A **38**, 2471 (1988).
[51] P. G. Browne and M. H. Dunn, J. Phys. B **6**, 1103 (1973).
[52] T. Kubota, Y. Morisaki, A. Ohsawa, and M. Ohuchi, J. Phys. D **25**, 613 (1992).
[53] A. V. Phelps, Phys. Rev. **99**, 1307 (1955).
[54] K. Tachibana, Phys. Rev. A **34**, 1007 (1986).
[55] J. H. Kolts and D. W. Setser, J. Chem. Phys. **68**, 4848 (1978).
[56] A. Bogaerts and R. Gijbels, Phys. Rev. A **52**, 3743 (1995).
[57] A. V. Phelps and J. P. Molnar, Phys. Rev. **89**, 1202 (1953).
[58] D. P. Lymberopoulos and D. J. Economou, J. Appl. Phys. **73**, 3668 (1993).
[59] N. B. Kolokolov and A. B. Blagoev, Phys. Usp. **36**, 152 (1993).
[60] A. V. Phelps, J. Appl. Phys. **76**, 747 (1994).
[61] N. Matsunami, Y. Yamamura, Y. Itikawa, N. Itoh, Y. Kazumata, S. Miyagawa, K. Morita, R. Shimizu, and H. Tawara, At. Data Nucl. Data Tables **31**, 1 (1984).
[62] J. A. Valles-Abarca and A. Gras-Marti, J. Appl. Phys. **55**, 1370 (1984).
[63] A. Bogaerts, M. van Straaten, and R. Gijbels, J. Appl. Phys. **77**, 1868 (1995).
[64] M. Grozeva (private communication).
[65] J. Mizeraczyk, Acta Phys. Hung. **54**, 71 (1983).
[66] J. Mizeraczyk, J. Phys. D **20**, 429 (1987).
[67] R. R. Arslanbekov, A. A. Kudryavtsev, and R. C. Tobin, Plasma Sources Sci. Technol. **7**, 310 (1998).
[68] S. Pfau, R. Kosakov, M. Otte, and J. Rohmann, Proceedings of XXIV ICPIG, Warsaw (1999), p. 262.
[69] N. Baguer, A. Bogaerts, and R. Gijbels, J. Appl. Phys. (in press).
[70] J. R. McNeil, G. J. Collins, and F. J. de Hoog, J. Appl. Phys. **50**, 6183 (1979).
[71] A. Bogaerts and R. Gijbels, J. Appl. Phys. **79**, 1279 (1996).